

**Impact of Local Structure on Halogen Ion Migration in Layered Methylammonium Copper Halide
Memory Devices**

Aniruddha Ray,^{†‡#} Beatriz Martín-García,^{†∇#} Alberto Martinelli,^{‡#} Davide Spirito,[§] Federico Locardi,^{¥‡}
Davide Altamura[♦], Cinzia Giannini[♦], Mirko Prato,^Δ Liberato Manna,^{†*} and Ahmed L. Abdelhady^{†*}

[†]Nanochemistry Department, ^ΔGraphene Labs and ^ΔMaterials Characterization Facility, Istituto Italiano di
Tecnologia, Via Morego 30, 16163 Genova, Italy

[‡]Dipartimento di Chimica e Chimica Industriale, Università degli Studi di Genova, Via Dodecaneso, 31, 16146,
Genova, Italy

[∇]CIC nanoGUNE, Tolosa Hiribidea 76, 20018 Donostia-San Sebastian, Basque Country, Spain.

[‡]SPIN-CNR, C.so Perrone 24, I-16152 Genova, Italy

[§]IHP—Leibniz-Institut für innovative Mikroelektronik, Im Technologiepark 25, D-15236 Frankfurt (Oder),
Germany

[¥]Physics and Chemistry of Nanostructures (PCN), Ghent University, Krijgslaan 281 - building S3 (Campus
Sterre), 9000 Gent, Belgium

[♦]Istituto di Cristallografia, Consiglio Nazionale delle Ricerche, v. Amendola 122/O, 70126 Bari, Italy

[#]Contributed equally.

^{*}Corresponding author(s): liberato.manna@iit.it and ahmed.abdelhady@iit.it

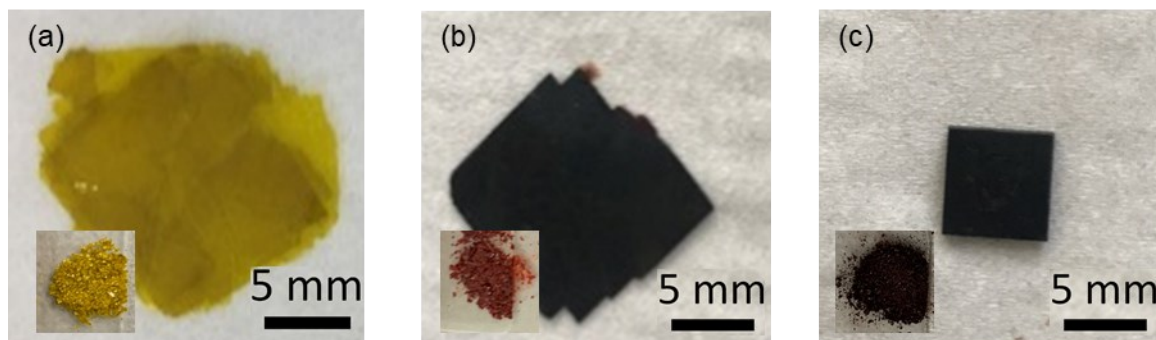


Figure S1. Photographs of the as-grown Cu-based crystals (a) Cu-1 and (b) Cu-2 and (c) Cu-3 and their ground powders in the insets.

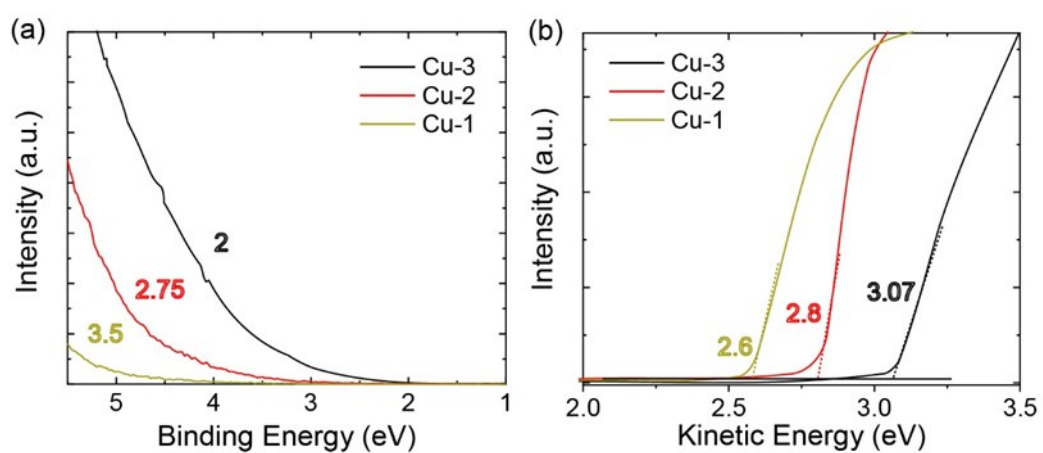


Figure S2. Zoomed-in sections of the uncalibrated UPS spectra for the 3 samples (a) Onset and (b) Cut-off regions

Differential Thermal Analysis/Thermogravimetric coupled with Gas Chromatography and Mass Spectrometry

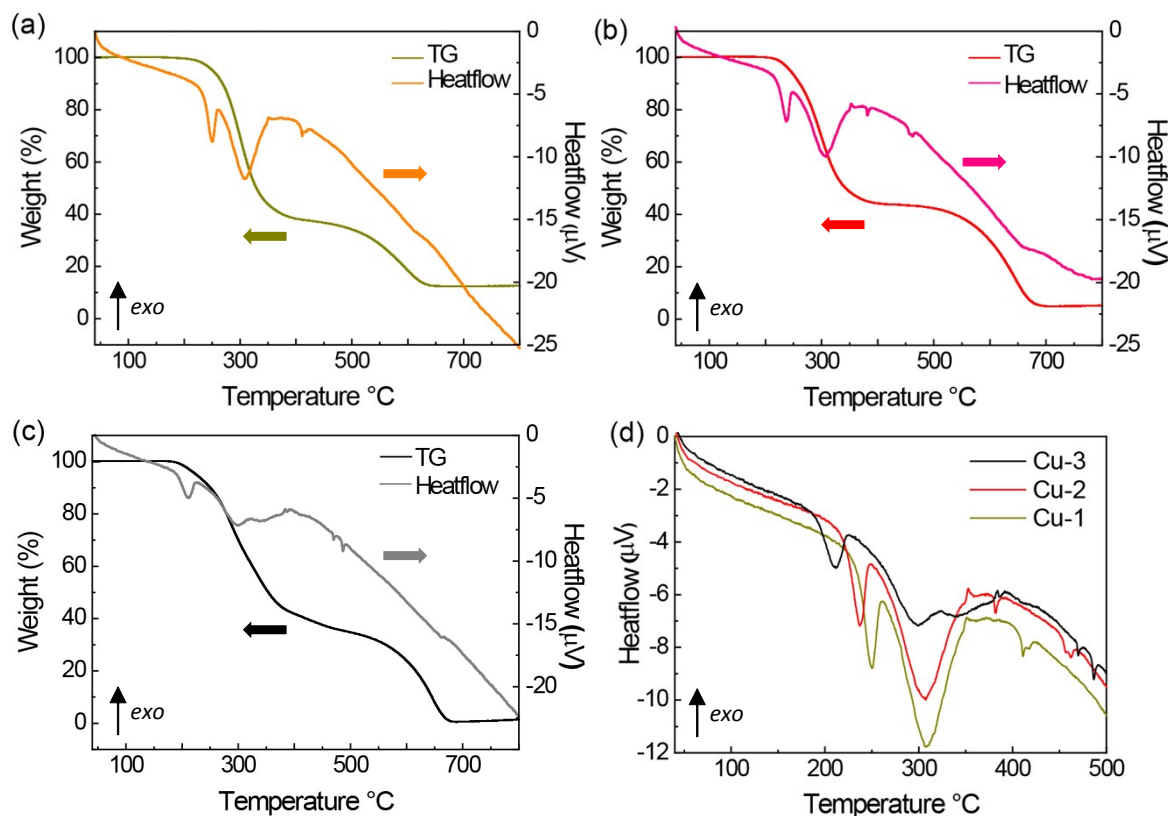


Figure S3. TG and DTA analyses for (a) Cu-1, (b) Cu-2 and (c) Cu-3. (d) Comparison of the DTA curves in the range 40 – 500 $^{\circ}\text{C}$.

DTA curves show a first endothermic peak, ascribing to the decomposition of the samples, that shifted to lower temperature increasing the Br amount; in particular, Cu-1 decomposed at 237 $^{\circ}\text{C}$ (T_{onset}), Cu-2 at 224 $^{\circ}\text{C}$ (T_{onset}) and Cu-3 at 198 $^{\circ}\text{C}$ (T_{onset}). This step is driven by the release of CH_3Cl and CH_3Br , as confirmed by the GC – MS analysis (Figure S4). This latter step is immediately followed by a second endothermic peak that becomes broader increasing the Br. A clear identification of the decomposition mechanism is not trivial but it is reasonable to assume that the contemporary formation of the $\text{N}(\text{CH}_3)_3$ and CuX_2 ($\text{X} = \text{Cl}$ and Br) takes place; the formation of the CuX may also occurred. Additional endothermic peak are present at $T > 400^{\circ}\text{C}$ that are ascribed to the melting point of the inorganic part (mainly CuX and CuX_2 species).

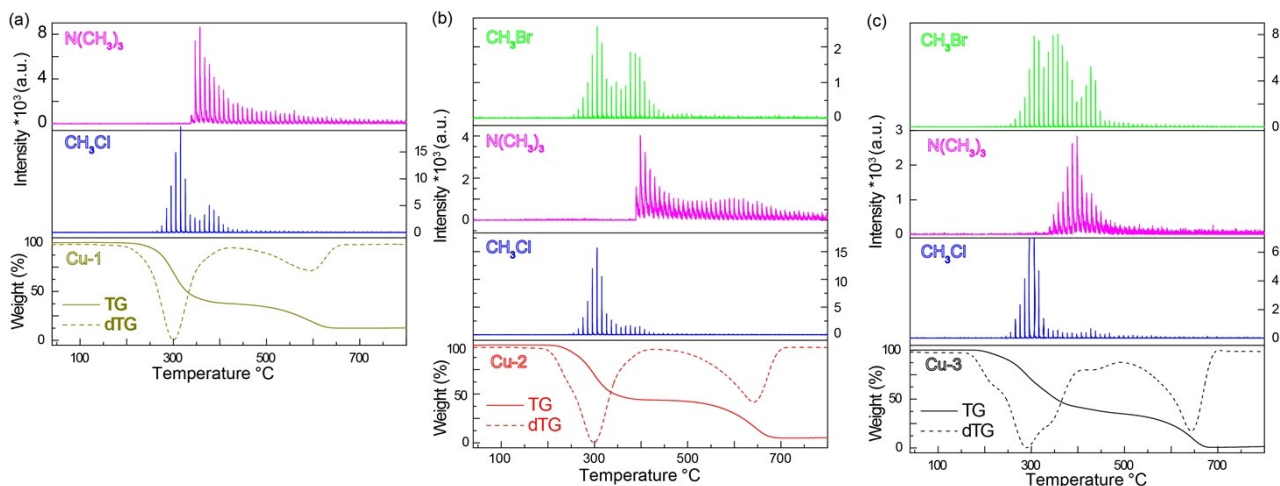


Figure S4. TG, dTG and evolved gas analyses (by means of GC – MS) for sample (a) Cu-1, (b) Cu-2 and (c) Cu-3. The released molecules were identified using the NIST mass spectra library; the comparison between the experimental and theoretical mass spectra are reported in Figure S5. The intensity of the identified molecules are normalized to the initial weight of the samples and, thus, are comparable. CH_3Cl decreases from Cu-1 to Cu-3, consistent with the presence of lower amount of Cl⁻; similarly, CH_3Br increases from Cu-2 to Cu-3. $\text{N}(\text{CH}_3)_3$ intensity progressively decreases indicating that the whole decomposition mechanism is modified by the introduction of Br⁻ in the lattice. Indeed, the dTG curves showed clearly as sample Cu-3 involved more steps respect to the other two samples.

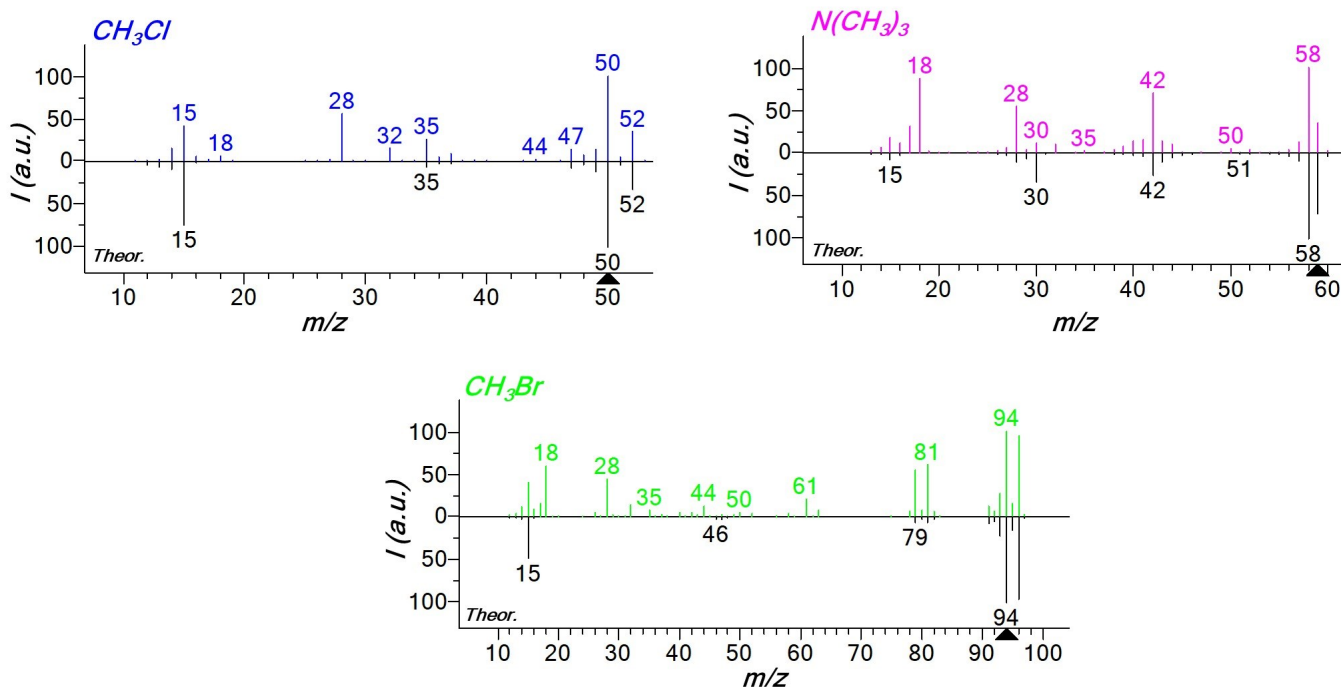


Figure S5. Comparison between theoretical (black) and representative experimental (coloured) mass spectra of the molecules released during the thermal analysis. The identification was carried out using the NIST mass spectra library.

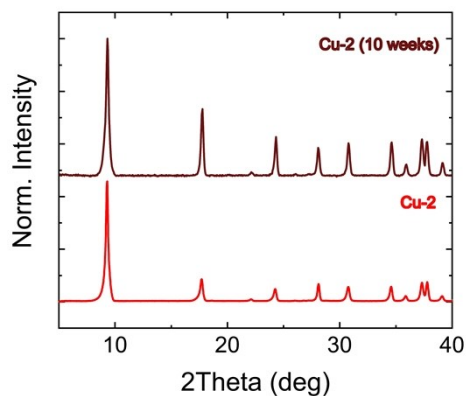


Figure S6. Laboratory XRPD diffractograms of (bottom) freshly ground Cu-2 crystal and (top) after storage in a vacuum oven kept at 40 °C for 10 weeks

Synchrotron X-ray powder diffraction (XRPD) and Pair Distribution Function (PDF) analyses

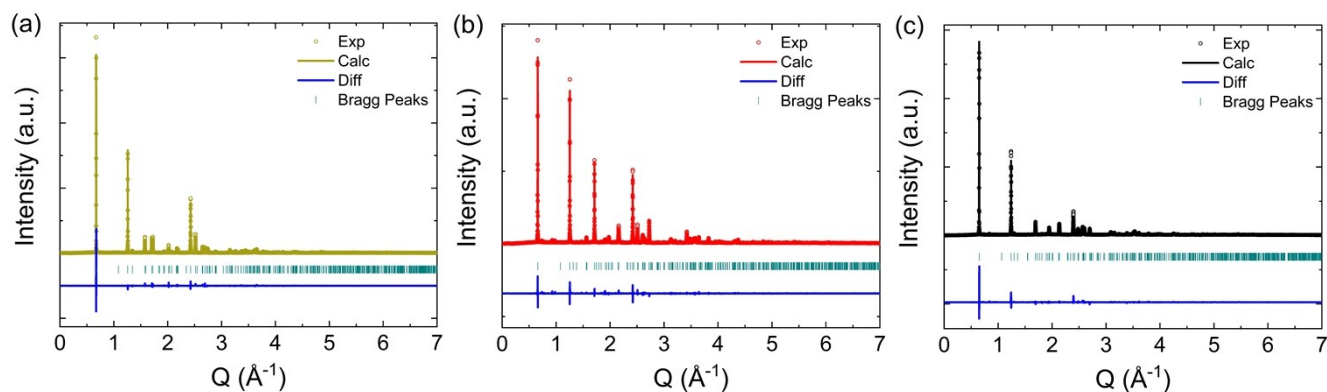


Figure S7. (a-c) Rietveld refinement plots of synchrotron XRPD data obtained for Cu-1, Cu-2, and Cu-3, respectively.

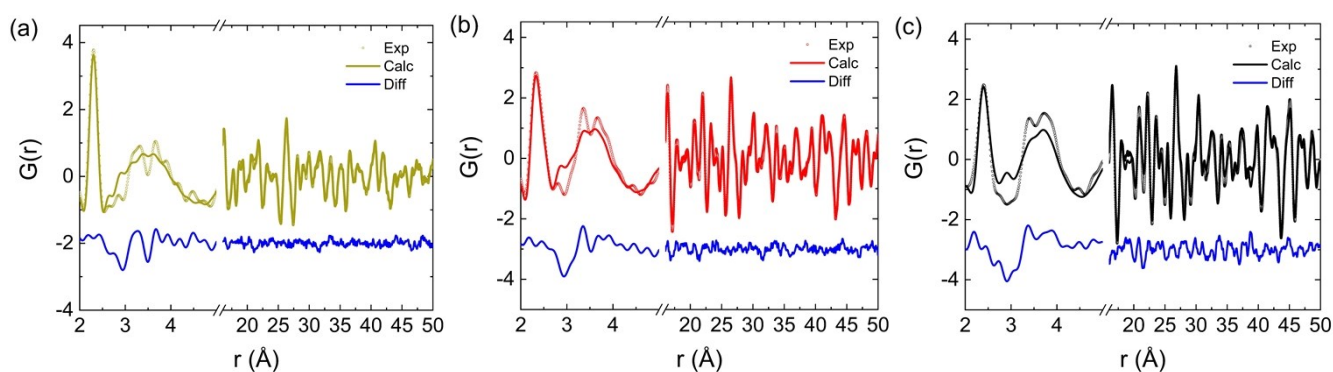


Figure S8. (a-c) $G(r)$ curves fitting (PDF data in the range 2 – 50 Å) for Cu-1, Cu-2, and Cu-3, respectively.

Devices Characterization

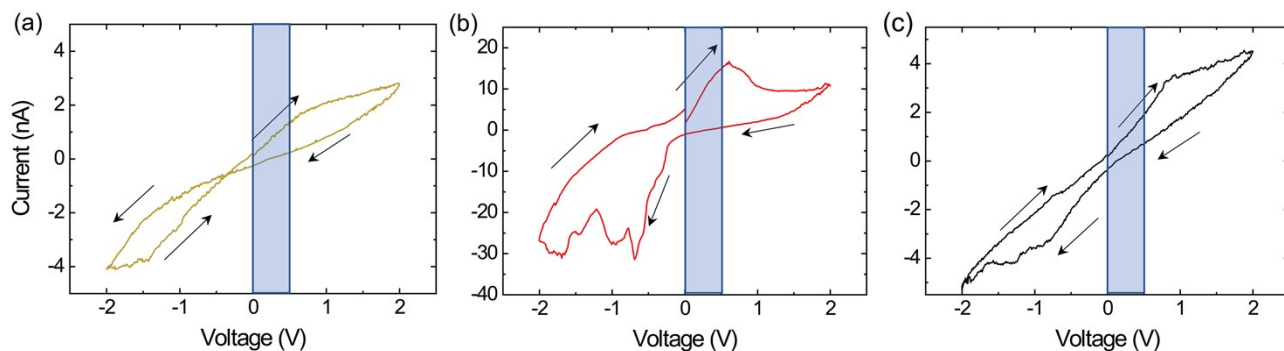


Figure S9. I–V cycle characteristics in linear scale for representative (a) Pt/Cu-1/Pt, (b) Pt/Cu-2/Pt and (c) Pt/Cu-3/Pt devices indicating with a shaded area the operational voltage range for the memristor read-out.

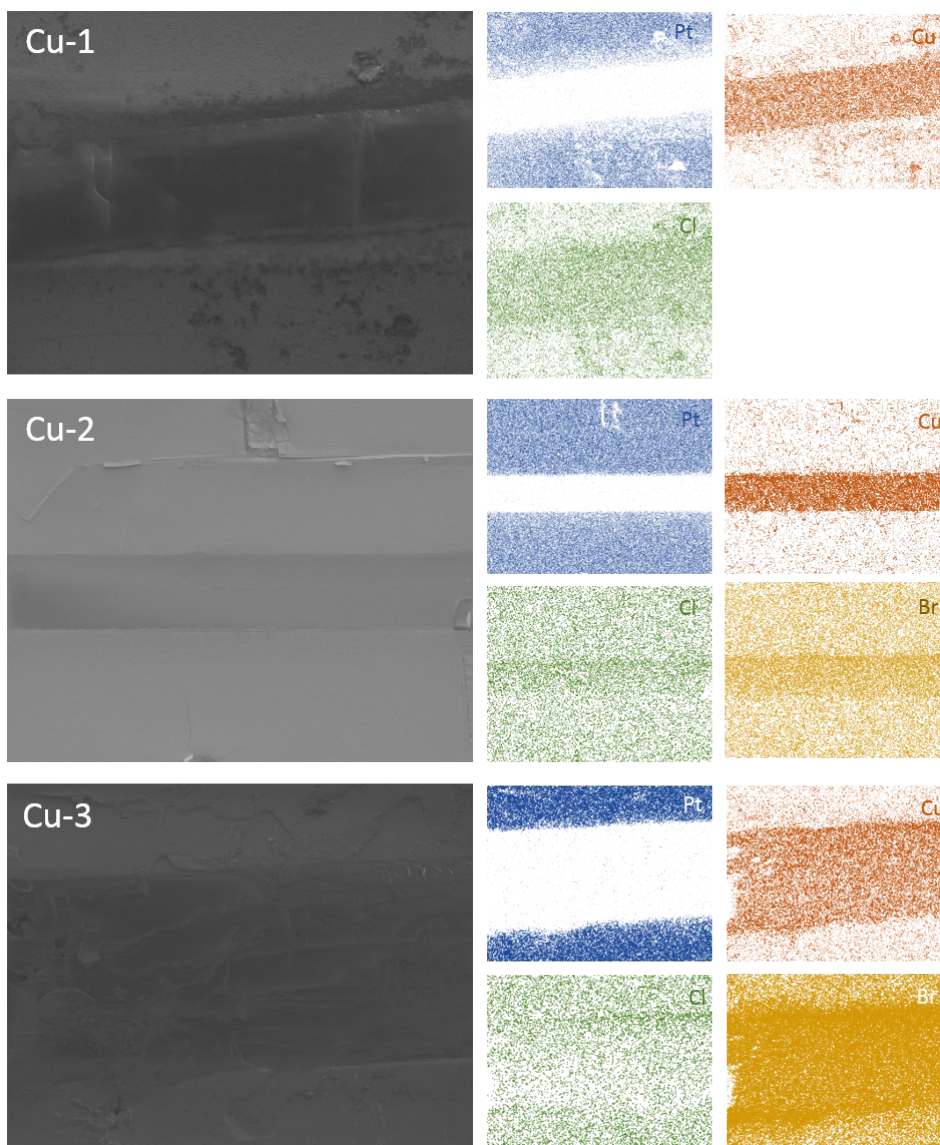


Figure S10. (a-c) Representative SEM-EDS maps of the devices after operation for Cu-1, Cu-2 and Cu-3, respectively. The spectral lines used for the EDS were: Pt (blue, $M = 2.05$ keV), Cu (orange, $L\alpha = 0.93$ keV), Cl (green, $K\alpha = 2.62$ keV) and Br (yellow, $L\alpha = 1.48$ keV).

We carried out scanning electron microscopy coupled to energy dispersive X-Ray spectroscopy (SEM-EDS) mapping of the devices after the set-reset measurements. In all the cases, the corresponding EDS maps of the Pt, Cu, Cl and Br indicate that there is neither Pt migration nor metallic Cu clusters formation during the device operation, since there is no signal of them in the conductive channel between the Pt electrodes. Therefore, the working mechanism in the device is the halide migration.

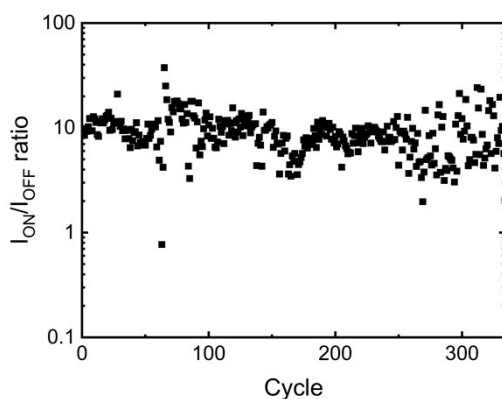


Figure S11. Endurance test of Cu-2 memory device in terms of ON/OFF ratio of the current measured with READ voltage of 0.1 V.

Note S1

With reference to Figure 6d-f in the main text (see Figure SX for the graph in linear scale), we observe that in Cu-1 sample, starting from 0 V to 2V, the current increases with the voltage (low resistance); then, during the sweep down from 2 V to 0 V, we observe a lower current (higher resistance) than in the sweep up. We continue the sweep down 0 V to -2 V, then we reverse it by increasing the voltage from -2 V to 0 V. In this loop, the absolute value of the current is higher in the sweep up than in the sweep down (lower resistance). The full cycle has an “8” shape, with a crossing, behavior that is denoted as “bipolar resistive switching”.¹⁻³ In Cu-2 and Cu-3 samples, where the Br is introduced, the behavior in the first part of the cycle (sweep up from 0 V to 2 V and down to 0 V) is similar, with the sweep up having a lower resistance than the sweep down. However, after passing 0 V, during the sweep down to -2 V the current increases (in absolute value) steeply, and when returning from -2 V to 0 V the current is smaller (higher resistance). This behavior is commonly referred to as “complementary resistive switching”⁴ and the observed hysteresis shape without crossing can be ascribed to local changes at interfaces due to the electric field⁵ and/or additional capacitive effects.⁶

To discuss the connection between the I-V curve patterns and the resistive switching mechanisms, we must first of all note that in perovskite materials several types of I-V characteristics have been observed³, and cannot

unambiguously discern the physical mechanism by itself.⁷ Furthermore, the choice of metals with different work function or ion solubility in the active material, and even the shape of the electrodes⁸ can be effective in determining the nature of the contact; thus, on one side the interpretation of the curves can be not straightforward, but on the other side this leaves ample room for contact optimization.⁸

As mentioned, in Cu-1 we observe bipolar switching, that can occur when there is an asymmetry in defect/vacancies concentration in the device induced by the voltage applied.⁶ It can be possible that the asymmetry generated cannot be structurally overcome, and it does not change to the complementary behavior.

In contrast, the complementary switching, observed in Cu-2 and Cu-3 is common in symmetric devices, as noted by Yang *et al.*⁹, where a key role is played by the dynamics of the distribution of vacancies in the material. The application of a voltage leads to an accumulation of vacancies at one electrode, inducing a high resistance on one side of the device. The application of an opposite bias will reverse the configuration.^{10,11} This behavior can be described as a self-limiting effect in the vacancy diffusion.^{4,12} The high/low resistance at the electrode can be also related to the formation of a Schottky junction, as noted in other layered materials such as MoS₂¹³, where the switching is controlled by sulfur vacancies dynamics. In this way, we can describe our Cu-2 and Cu-3 devices as comprised of a resistive medium, the Cu layered crystal, with two Schottky barriers at the metal junctions (Pt contacts), resulting in the small current (order of nA) measured in the device. After biasing the device, the drift of ions and vacancies to the contacts will pin the Fermi level at the junction and affect the Schottky barrier height, resulting in a configuration with a diode in forward bias for positive voltage. This ion/vacancies redistribution in the device may be reflected in the I-V curves by a shift of the current minimum values from zero voltage.^{14,15} When the bias is reduced and finally reversed, the overall doping distribution will swap to the opposite contacts, and the device will be in forward bias for negative voltage. This behavior is likely to be enhanced in case of high ion and/or vacancy mobility, *i.e.* in Cu-2, which also presents a larger shift in the I-V characteristics^{14,15} as detailed in the main text.

References

- 1 M. Lanza, H. S. P. Wong, E. Pop, D. Ielmini, D. Strukov, B. C. Regan, L. Larcher, M. A. Villena, J. J. Yang, L. Goux, A. Belmonte, Y. Yang, F. M. Puglisi, J. Kang, B. Magyari-Köpe, E. Yalon, A. Kenyon, M. Buckwell, A. Mehonic, A. Shluger, H. Li, T. H. Hou, B. Hudec, D. Akinwande, R. Ge, S. Ambrogio, J. B. Roldan, E. Miranda, J. Suñe, K. L. Pey, X. Wu, N. Raghavan, E. Wu, W. D. Lu, G. Navarro, W. Zhang, H. Wu, R. Li, A. Holleitner, U. Wurstbauer, M. C. Lemme, M. Liu, S. Long, Q. Liu, H. Lv, A. Padovani, P. Pavan, I. Valov, X. Jing, T. Han, K. Zhu, S. Chen, F. Hui and Y. Shi, *Adv. Electron. Mater.*, 2019, **5**, 1–28.
- 2 R. Waser, D. Ielmini, H. Akinaga, H. Shima, H.-S. P. Wong, J. J. Yang and S. Yu, *Resist. Switch.*, 2016, 1–30.

- 3 B. Li, W. Hui, X. Ran, Y. Xia, F. Xia, L. Chao, Y. Chen and W. Huang, *J. Mater. Chem. C*, 2019, **7**, 7476–7493.
- 4 F. Nardi, S. Balatti, S. Larentis, D. C. Gilmer and D. Ielmini, *IEEE Trans. Electron Devices*, 2013, **60**, 70–77.
- 5 R. Zazpe, P. Stoliar, F. Golmar, R. Llopis, F. Casanova and L. E. Hueso, *Appl. Phys. Lett.*, 2013, **103**, 073114.
- 6 R. Schmitt, J. Spring, R. Korobko and J. L. M. Rupp, *ACS Nano*, 2017, **11**, 8881–8891.
- 7 A. Solanki, A. Guerrero, Q. Zhang, J. Bisquert and T. C. Sum, *J. Phys. Chem. Lett.*, 2020, **11**, 463–470.
- 8 H. Y. Peng, L. Pu, J. C. Wu, D. Cha, J. H. Hong, W. N. Lin, Y. Y. Li, J. F. Ding, A. David, K. Li and T. Wu, *APL Mater.*, , DOI:10.1063/1.4827597.
- 9 H. Z. Zhang, D. S. Ang, K. S. Yew and X. P. Wang, *Appl. Phys. Lett.*, 2016, **108**, 083505.
- 10 P. K. Radtke, A. L. Hazel, A. V Straube and L. Schimansky-Geier, *New J. Phys.*, 2017, **19**, 093007.
- 11 Y. Yang, P. Sheridan and W. Lu, *Appl. Phys. Lett.*, 2012, **100**, 203112.
- 12 D. Ielmini and V. Milo, *J. Comput. Electron.*, 2017, **16**, 1121–1143.
- 13 D. Li, B. Wu, X. Zhu, J. Wang, B. Ryu, W. D. Lu, W. Lu and X. Liang, *ACS Nano*, 2018, **12**, 9240–9252.
- 14 X. Guan, W. Hu, M. A. Haque, N. Wei, Z. Liu, A. Chen and T. Wu, *Adv. Funct. Mater.*, 2018, **28**, 1–11.
- 15 H. Duim, H. H. Fang, S. Adjokatse, G. H. Ten Brink, M. A. L. Marques, B. J. Kooi, G. R. Blake, S. Botti and M. A. Loi, *Appl. Phys. Rev.*, , DOI:10.1063/1.5088342.